frontiers | Frontiers in Materials

ORIGINAL RESEARCH
published: 28 April 2022
doi: 10.3389/fmats.2022.879711

Strong Perpendicular Anisotropy and Anisotropic Landé Factor in Bismuth-Doped Thulium Garnet Thin Films

Xiuye Zhang[1], Lichuan Jin[1], Dainan Zhang[1], Bo Liu[2]*, Hao Meng[2], Lei Zhang[1], Zhiyong Zhong[1] and Xiaoli Tang[1]*

[1]State Key Laboratory of Electronic Thin Films and Integrated Devices, University of Electronic Science and Technology of China, Chengdu, China, [2]Key Laboratory of Spintronics Materials, Devices and Systems of Zhejiang Province, Hangzhou, China

With the development of spintronics, garnet films with perpendicular magnetic anisotropy (PMA) have been attracting the attention of researchers for decades. In this work, bismuth-doped thulium iron garnet ($Tm_2BiFe_5O_{12}$, TmBiIG) films of varying thickness having strong PMA effect were fabricated on substituted $Gd_3Ga_5O_{12}$ (sGGG) (111) substrates using the pulsed laser deposition (PLD) technique. Crystallographic characterization and magnetic properties of TmBiIG films were investigated using high-resolution scanning transmission electron microscopy, X-ray diffraction, vibrating sample magnetometry, and broadband ferromagnetic resonance (FMR). A high perpendicular anisotropic field of $H_\perp$ = 4,445 ± 7.5 Oe in a 10-nm-thick film and $H_\perp$ = 4,582 ± 7.7 Oe in a 30-nm-thick film at room temperature were obtained and analyzed in detail. Surprisingly, an additional spin-wave mode was observed in the in-plane FMR spectra. The discrepancy between in-plane and the out-of-plane Landé g-factors established a correlation with the PMA effect in the TmBiIG films. The Landé g-factor of the TmBiIG films is much lower than that of free electrons, indicating that the strong spin–orbit coupling is caused by Tm and Bi heavy elements. The Gilbert damping factor α changed from 0.007 to 0.012 in various thicknesses of TmBiIG films.

Keywords: bismuth-doped thulium iron garnet, perpendicular magnetic anisotropy, spintronic materials, Landé g-factor, ferromagnetic resonance spectrum

Edited by:
Jijie Huang,
Sun Yat-sen University, China

Reviewed by:
Yanda Ji,
Nanjing University of Aeronautics and Astronautics, China
Di Zhang,
Los Alamos National Laboratory (DOE), United States

****Correspondence:***
Lichuan Jin
lichuanj@uestc.edu.cn
Bo Liu
liubo_sm@163.com

Specialty section:
This article was submitted to Thin Solid Films, a section of the journal Frontiers in Materials

Received: *20 February 2022*
Accepted: *28 March 2022*
Published: *28 April 2022*

Citation:
Zhang X, Jin L, Zhang D, Liu B, Meng H, Zhang L, Zhong Z and Tang X (2022) Strong Perpendicular Anisotropy and Anisotropic Landé Factor in Bismuth-Doped Thulium Garnet Thin Films. Front. Mater. 9:879711. doi: 10.3389/fmats.2022.879711

INTRODUCTION

Spintronics based on magnetic garnets is a potential choice for data storage, logical computation, and next-generation sensing. Ferrimagnetic garnets, such as yttrium iron garnet (Sokolov et al., 2016) ($Y_3Fe_5O_{12}$, YIG) or thulium iron garnet ($Tm_3Fe_5O_{12}$, TmIG) have been extensively studied for spin transport and spin interactions, such as inverse spin Hall effect (Li et al., 2020) (ISHE), spin Seebeck effect (Kikkawa et al., 2013) (SSE), spin–orbit torque (Avci et al., 2017) (SOT) switching, and topological hall effect (Ahmed et al., 2019; Shao et al., 2019), due to their small Gilbert damping factor (10^{-4}–10^{-2}), narrow ferromagnetic resonance linewidth, and perpendicular magnetic anisotropy (PMA) effect. Recently, Avci et al. (2017) developed new devices for regulating SOTs in a TmIG/Pt heterostructure grown on (111)-oriented gadolinium gallium garnet ($Gd_3Ga_5O_{12}$,

GGG) with the PMA effect. This observation may lead to a new direction of research that can reduce the energy consumption in integrated devices and can demonstrate the importance of investigating new garnets having a reliable and powerful PMA effect.

The method for obtaining a strong PMA effect in garnet films is to introduce a large uniaxial anisotropy, K_u, composed of stress-induced perpendicular anisotropy K_u^{λ} and growth-induced anisotropy K_u^{g}, which are related to the lattice mismatch, magnetostriction constant, and interaction between the ions (Hansen and Witter, 1985). There are several ways to obtain ferrimagnetic garnet films with a strong PMA effect, such as doping with Bi (Hansen et al., 1983; Hansen and Krumme, 1984; Hansen and Witter, 1985; Soumah et al., 2018; Lin et al., 2020), introducing extra K_u^{g}, substituting other rare-earth elements (Tang et al., 2016; Avci et al., 2017; Wu et al., 2018), using a large magnetostriction constant to improve K_u^{λ}, or changing the substrate materials (Tang et al., 2016; Fu et al., 2017; Ciubotariu et al., 2019) to enlarge K_u^{λ} by creating a greater lattice mismatch. Ultrathin films manufactured in the GGG (111)/TmIG system exhibit the PMA effect, owing to the great negative magnetostriction constant of the TmIG (Tang et al., 2016; Vilela et al., 2020) compared to the YIG (Sokolov et al., 2016; Fu et al., 2017).

In this work, bismuth-doped thulium iron garnet ($Tm_2BiFe_5O_{12}$, TmBiIG) films of varying thicknesses with a strong PMA effect were fabricated on 5 mm × 5 mm × 0.5 mm sGGG (111) substrates using the pulsed laser deposition (PLD) technique. The value of the perpendicular anisotropic field in different film thicknesses was determined by ferromagnetic resonance measurements. Due to the strong PMA effect of the film (Farle, 1998), an extra spin-wave mode was observed in the in-plane magnetized condition when applied magnetic field H is smaller than the net perpendicular anisotropy field $4\pi M_{eff}^{\perp}$. This has also been observed in some other materials having a strong PMA effect (Barsukov et al., 2014; Tivakornsasithorn et al., 2014). Moreover, the difference between the in-plane and the out-of-plane Landé g-factors can be obtained from FMR spectrum analysis in correlation with the PMA effect in the TmBiIG films. Furthermore, unlike other rare-earth elements and transition metals (Woltersdorf et al., 2009), the doped Bi^{3+} ions did not enlarge the Gilbert damping factor α as compared to the TmIG/sGGG (Ciubotariu et al., 2019) system, whose values are 0.007–0.012 in different thickness TmBiIG. This strong perpendicular anisotropy field and relatively low Gilbert damping lay a solid foundation for future study on spintronics materials.

MATERIALS AND METHODS

In our experiments, a 2-inch $Tm_2BiFe_5O_{12}$ ceramic target with high purity was fabricated by a standard solid state reaction method of Tm_2O_3 (99.999%), Bi_2O_3 (99.999%), and Fe_2O_3 (99.999%). Before the growth, a mixture of concentrated 10 ml sulfuric acid and 10 ml hydrogen peroxide was prepared, and the sGGG substrate was immersed for 15 min to remove the oxide impurities on the surface. Then sGGG substrate was soaked in acetone and alcohol, respectively, for ultrasonic cleaning to obtain a clean substrate surface. Before depositing the films, the distance between the target and the substrate was adjusted to 70 mm. The wavelength of the KrF excimer laser used in PLD was 248 nm. Laser intensity and frequency were set to 300 mJ (2.4 J/cm^2) and 5 Hz, respectively. The base vacuum level of the chamber was 8×10^{-6} Pa. During the pre-deposition process, the temperature in the chamber was raised from room temperature to 750°C at a rate of about 12°C/min. At the same time, the oxygen pressure was set to 1 Pa in order to form a high-quality TmBiIG film. Under the aforementioned conditions, the growth rate of the film was about 2 nm/min. After the deposition, the films were transferred to a thermal annealing system for recrystallization at 800°C in air atmosphere for 1 h, and the heating rates and cooling rates are 60°C/min and 4.33°C/min, respectively.

TmBiIG films were characterized by a high-resolution X-ray diffractometer (HRXRD, Bede D1), high-resolution scanning transmission electron microscopy (STEM, FEI Talos F200X), atomic force microscope (AFM, PARK-XE7), vibrating sample magnetometry (VSM, USA LakeShore 8,603), and angular-resolved FMR measurements. The FMR spectrum was obtained by sweeping the magnetic field at a fixed microwave frequency. The derivative of microwave absorption power and the static magnetic field was defined as the intensity of the FMR spectrum, which was attained by applying a static magnetic field in-plane and out-of-plane. Coplanar waveguide (CPW) and short circuit antenna structures were composed of 20 nm Ta and 200 nm Au manufactured by photolithography. All the measurements were conducted at room temperature.

RESULTS AND DISCUSSION

The surface morphology characterization of a 20-nm-thick TmBiIG film sample measured in the contact mode is shown in **Figure 1A**. The root-mean-square (rms) roughness of the film over a 2 μm × 2 μm scanned area is 0.3 nm, which indicates a smooth film surface. All samples in this work show a similar rms roughness. The in-plane XRD result along (20-2) of a 30-nm-thick film is shown in **Figure 1B**, the position of the diffraction peak corresponds to that in the study by Wu et al. (2018). No discernible separation of the peaks of TmBiIG films and sGGG substrates was observed, which means the sample grew coherently on the substrate through the strain. Peaks from thinner samples could not be resolved using XRD. However, considering the thickest sample in the study grow coherently on the substrate and the film of each thickness used in this work exhibits the PMA effect, all thickness samples are supposed to show a similar in-plane XRD pattern. **Figure 1C** displays a series of HRXRD patterns for the TmBiIG films grown on the (111) sGGG substrates at various thicknesses. The radiation line of the HRXRD is Cu-Kα. A bare substrate diffraction pattern is performed for comparison, revealing the contributions from $K\alpha_2$ and $K\alpha_1$ (Illig et al., 2013), which split the main (444) reflection of the substrates. According to the XRD patterns, the thickness of the TmBiIG has an obvious effect on the

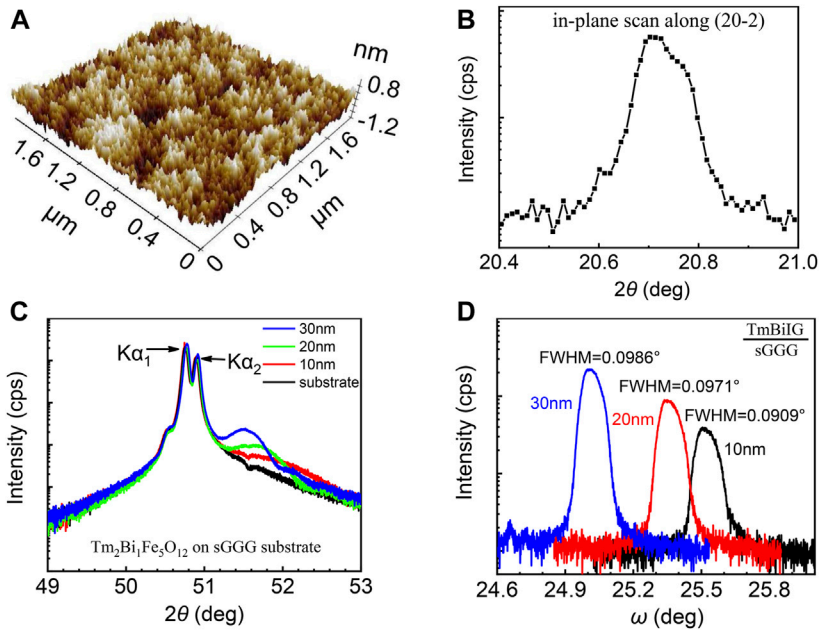

FIGURE 1 | (A) AFM surface morphology of a 20-nm-thick TmBiIG film in a 2 μm × 2 μm region with rms roughness of 0.3 nm, demonstrating the ultra-flat surface. Crystallographic characterization results for the TmBiIG films; **(B)** HRXRD in-plane scan of the 30-nm-thick sample along the (20-2) direction; **(C)** HRXRD ω–2θ scans of the (444) plane of the TmBiIG/sGGG (111), and **(D)** rocking curve of the TmBiIG (444) for various film thicknesses.

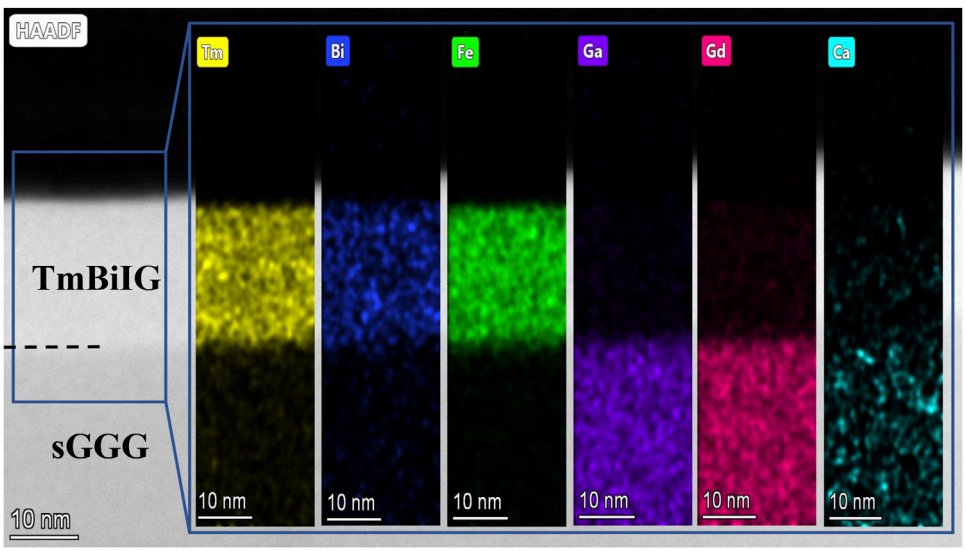

FIGURE 2 | HAADF-STEM image of the 20-nm-thick TmBiIG/sGGG cross-sectional structure. The black line of dashes shows the boundary between film and substrate. EDS exhibits the location distribution of the Tm, Bi, Fe, Ga, Gd, and Ca elements by comparing different colors.

crystalline structure. With the decrease in the film thickness, the (444) diffraction peak of TmBiIG at an angle of 2θ becomes larger, indicating a more compressed lattice in the direction of growth, which results in a smaller lattice constant in the film's normal direction. Through Bragg's laws, the lattice spacing was deduced from the XRD results, and then the lattice parameter was calculated. The out-of-plane strain states $\varepsilon_{\perp}$ of 10-, 20-, and 30-nm-thick films are −1.56%, −1.45%, and −1.13%, respectively. Considering all samples are strained without relaxation, the value of in-plane strain states $\varepsilon_{\parallel}$ was 0.54%. **Figure 1D** demonstrates a series of narrow rocking curves of the TmBiIG (444) peak (FWHM = 0.0909–0.0986), which confirms its good crystallinity.

Figure 2 shows a high angle annular dark field scanning transmission electron microscopy (HAADF-STEM) image of

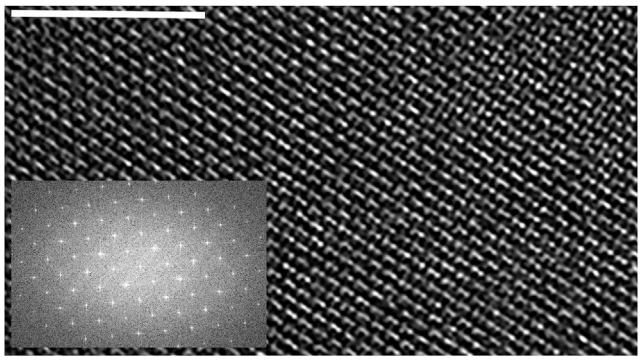

FIGURE 3 | HR-TEM image from a 20-nm-thick TmBiIG/sGGG cross-sectional structure. The white scale bar corresponds to 5 nm. Inset shows the FFT from the image.

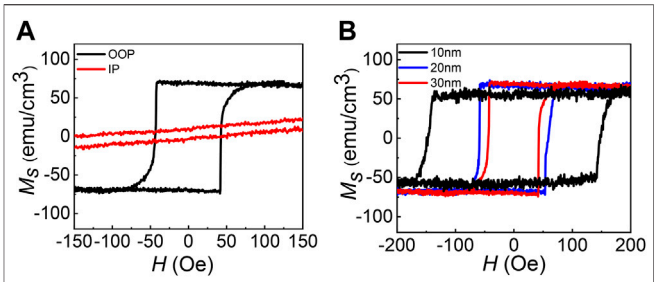

FIGURE 4 | (A) Out-of-plane (black line) and in-plane (red line) hysteresis loops of a 30-nm-thick sample in narrow range. **(B)** Out-of-plane hysteresis loop of 10-, 20-, and 30-nm-thick films in the narrow range. The paramagnetic contribution from the substrate sGGG has been removed in the raw data.

the 20-nm-thick sample. The line of dashes in **Figure 2** reveals the boundary between the TmBiIG film and the sGGG substrate, identified by an energy dispersive spectrometer (EDS) surface scan. Tm, Bi, and Fe elements in the film and Gd, Ga, and Ca elements in the substrate were verified, exhibiting the slight diffusion phenomenon of the above five atoms at both ends of the interface. **Figure 3** demonstrates an image of a high-resolution transmission electron microscope (HR-TEM) of the cross section from the 20-nm-thick TmBiIG film grown on sGGG, and a periodic lattice is clearly observed illustrating the good crystalline quality of the film. The well-ordered atomic structure and sharp diffraction spots illustrate good epitaxial growth of TmBiIG (111) on sGGG (111), and there is no visible dislocation or cracking in the film, even due to the in-plane strain.

In the existing works (Kubota et al., 2013; Zanjani and Onbasli, 2019), the film will be subjected to tensile strain when the film lattice constant a_{film} is less than the substrate lattice constant a_{sub}. The lattice constant of the TmBiIG film is smaller than the lattice constant of the sGGG substrate, inducing a tensile strain in the film. This is the source of the strong PMA effect of the film. To verify the strong PMA effect in the TmBiIG films, VSM measurements were performed on the same sample of TmBiIG films mentioned before. **Figure 4A** displays the in-plane and the out-of-plane hysteresis loops for the 30-nm-thick sample in a narrow magnetic field range. The out-of-plane hysteresis loop is squared and saturated in a small magnetic field, while the in-plane hysteresis loop does not saturate even with the maximum magnetic field (about 2000 Oe) of the instrument (not shown here), thereby exhibiting a hard-axis behavior. The out-of-plane hysteresis loop in **Figure 4B** exhibits the coercivity (H_C) and the saturation magnetization (M_S) per unit volume in the films with varying thicknesses. The saturation magnetization of 10-, 20-, and 30-nm-thick films are about 55, 67, and 71 emu/cm^3, respectively.

In the TmBiIG/sGGG system, the main contributors to the effective anisotropy energy density are shape anisotropy K_{shape}, uniaxial anisotropy K_u (commonly expressed as K_2 in other literature), and magnetocrystalline anisotropy K_1 (commonly expressed as K_4 in other literature). Generally, perpendicular anisotropy in thin films is due to the sum of the perpendicular anisotropy energy $K_\perp$ ($K_u + K_1$), which is large enough to overcome the shape anisotropy energy K_{shape}. In this article, we used angular-resolved FMR measurements and VSM to determine the total perpendicular anisotropy energy of the TmBiIG films. The angle-dependent Smith–Suhl method for the arbitrary orientation of the applied magnetic field is used to deduce the ferromagnetic resonance condition in this work (Farle, 1998; Shaw et al., 2015; Ciubotariu et al., 2019):

$$\left(\frac{\omega_r}{\gamma}\right)^2 = \frac{1}{(M_S \sin\theta)^2}\left(F_{\theta\theta}F_{\varphi\varphi} - F_{\theta\varphi}^2\right). \tag{1}$$

Eq. 2 displays the free energy of the TmBiIG film:

$$\begin{aligned} F = {} & \frac{1}{2}\mu_0 M_S^2 \cos^2\theta - K_u \cos^2\theta - \frac{1}{2}K_{1\perp}\cos^4\theta \\ & - \frac{1}{8}K_{1\parallel}(3 + \cos 4\varphi)\sin^4\theta \quad - \mu_0 M_S H(\cos\theta\cos\theta_H \\ & + \cos(\varphi - \varphi_H)\sin\theta\sin\theta_H), \end{aligned} \tag{2}$$

where (θ, φ) and (θ_H, φ_H) are the polarization angle and in-plane azimuthal angle of magnetic moment and static magnetic field, respectively. γ is the gyromagnetic ratio and μ_0 is the vacuum permeability. When θ (θ_H) is 90 (0) degrees, the magnetic moment (static magnetic field) is considered as in-plane (out-of-plane). In **Eq. 2**, the first term is the demagnetization energy, the second term is the uniaxial anisotropy energy, the third and fourth terms are the magnetocrystalline anisotropy energy, and the fifth term is the Zeeman energy. We have measured the FMR spectrum of 10- and 30-nm-thick TmBiIG samples in in-plane and out-of-plane, respectively, shown in **Figure 5**, and in-plane angular FMR measurements (not shown here) exhibit the resonance field $H_{R\parallel}$ that has barely any variation, indicating that the $K_{1\parallel}$ of the films can be neglected. The in-plane ferromagnetic resonance condition and the out-of-plane ferromagnetic resonance condition can be derived from **Eqs 1**, **2**, as follows:When $\theta = \theta_H = 0^\circ$,

$$\frac{\omega_{r\perp}}{\gamma} = H_{R\perp} - 4\pi M_S + \frac{2(K_u + K_{1\perp})}{M_S}. \tag{3}$$

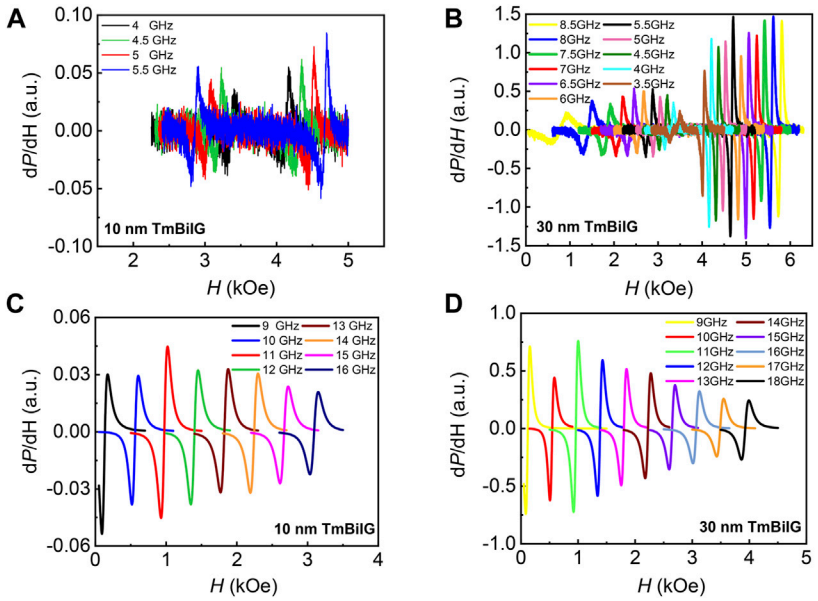

FIGURE 5 | FMR measurement of the TmBiIG film. In-plane ferromagnetic resonance spectra of **(A)** 10- and **(B)** 30-nm-thick samples. Out-of-plane ferromagnetic resonance spectra of **(C)** 10 nm thickness in 9–16 GHz (1 GHz interval) and **(D)** 30 nm thickness in 9–18 GHz (1 GHz interval).

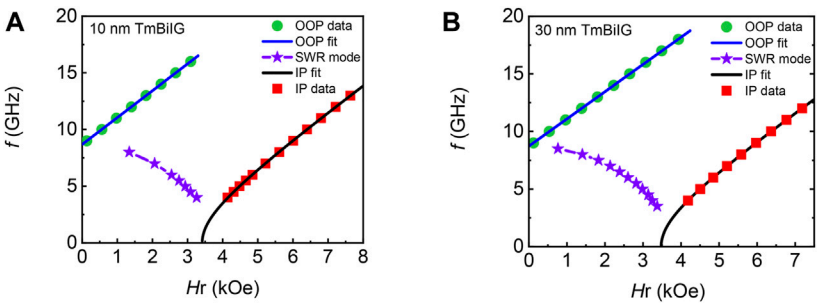

FIGURE 6 | Resonance magnetic field dependence on the frequency in **(A)** 10- and **(B)** 30-nm-thick films. An extra spin-wave mode (SWR) was detected in the in-plane ferromagnetic resonance spectra.

When $\theta = \theta_H = 90^\circ$,

$$\frac{\omega_{r\parallel}}{\gamma} = \sqrt{H_{R\parallel}\left(H_{R\parallel} + 4\pi M_S - \frac{2K_u}{M_s}\right)}. \quad (4)$$

Moreover,

$$4\pi M_{eff}^{\perp} = 4\pi M_s - \frac{2K_u}{M_s} - \frac{2K_{1\perp}}{M_s}, \quad (5)$$

$$4\pi M_{eff}^{\parallel} = 4\pi M_s - \frac{2K_u}{M_s}, \quad (6)$$

where $4\pi M_{eff}^{\perp}$ and $4\pi M_{eff}^{\parallel}$ extracted from the in-plane and the out-of-plane fitting curves, respectively, are as shown in **Figures 6A,B**. Meanwhile, the net perpendicular anisotropy field is defined as $4\pi M_{eff}^{\perp}$. A negative value of $4\pi M_{eff}^{\perp}$ explains that the perpendicular anisotropy energy overcomes the demagnetization energy and makes the residual magnetic moment orient out-of-plane. Furthermore, perpendicular anisotropic field $H_\perp$ were 4,445 ± 7.5 Oe and 4,582 ± 7.7 Oe in the 10- and 30-nm-thick films, respectively, from **Eq. 7**.

$$H_\perp = 4\pi M_s - 4\pi M_{eff}^{\perp}. \quad (7)$$

However, the experimental results show that the perpendicular anisotropic field $H_\perp$ of the 10-nm-thick film is slightly smaller than that of the 30-nm-thick film. This is due to the $4\pi M_S$ in the 10-nm-thick film being smaller than that in the 30-nm-thick film, which is shown in **Figure 4B**.

The comparison of the $H_\perp$ value between the TmBiIG/sGGG system and other ferrimagnetic garnet systems are shown in **Table 1**. It should be noted that the $H_\perp$ value in the TmBiIG/sGGG system is larger than that in the TmIG/sGGG system when the film has the same thickness (10 nm). This is due to the extra growth-induced anisotropy introduced by Bi doping. As a heavy

TABLE 1 | Comparison of magnetic anisotropy parameters based on the recent works. Partial reference data have been converted from the SI units to the CGS units in the article. It should be pointed out that the sGGG* listed in the table has a larger lattice constant than the substrate used in this work.

Samples	Thickness (nm)	Substrates	$4\Pi M_S$ (Oe)	$H_\perp$(Oe)	$K_\perp$(J/m^3)
YIG, Sokolov et al. (2016)	84	GGG	1750	−950	-0.7×10^4
YIG, Tang et al. (2016)	—	sGGG*	—	1,075	—
TMIG, Wu et al. (2018)	24.5	GGG	1,244	1734	0.9×10^4
TMIG, Tang et al. (2016)	10	sGGG	—	3,645	—
YBIIG, Soumah et al. (2018)	—	GGG	1,600	−290	-0.2×10^4
YBIIG, Soumah et al. (2018)	—	sGGG	1720	2010	1.3×10^4
TMBIIG	10	sGGG	779	4,445	1.4×10^4
TMBIIG	30	sGGG	892	4,582	1.6×10^4

TABLE 2 | Gyromagnetic ratio and Landé g-factor under in-plane and out-of-plane magnetized condition of the TmBiIG film with various thicknesses.

Thickness (nm)	$(\frac{\gamma}{2\pi})_\perp$ (GHz/kOe)	$(\frac{\gamma}{2\pi})_\parallel$ (GHz/kOe)	$g_\perp$	$g_\parallel$	$\Delta\mu_L/\mu_S$
10	2.37 ± 0.003	2.33 ± 0.002	1.69 ± 0.002	1.64 ± 0.002	0.025
20	2.40 ± 0.001	2.37 ± 0.003	1.71 ± 0.002	1.69 ± 0.002	0.01
30	2.37 ± 0.003	2.29 ± 0.004	1.69 ± 0.002	1.67 ± 0.001	0.01

element with strong spin–orbit interaction, Bi^{3+} ions have a profound influence on the local symmetry, super-exchange interaction, and spin–orbit coupling in the nearby Fe^{3+} ions. The order of priority for the Bi^{3+} ions in the dodecahedron position affects the uniaxial component of free energy of the adjacent Fe^{3+} ions in the octahedron and the tetrahedron positions, thus resulting in an additional magnetic anisotropy (Hansen and Witter, 1985).

As shown in **Figures 5A,B**, a special spin-wave mode exists at low frequencies and for low magnetic fields in all thickness films, which is also observed in other materials due to the strong perpendicular anisotropy (Barsukov et al., 2014; He et al., 2016; Glowinski et al., 2017; Devolder et al., 2018). This special spin mode was observed using the in-plane FMR measurements and is usually known as the smallest spin mode in bubble films (Portis, 1963; Dötsch et al., 1978). Unlike the Kittel mode, the magnitude of the resonance field is inversely related to the resonance frequency as this spin-wave mode occurs when the magnetic moment is not fully oriented in the in-plane, indicating that the magnetic moments are not processed uniformly (Hoekstra et al., 1977; Dötsch et al., 1978).

From the fitting analysis in **Eqs 3**, **4**, the gyromagnetic ratio of the in-plane and the out-of-plane magnetized of various thicknesses of the TmBiIG film is obtained. The values of $(\frac{\gamma}{2\pi})_\perp$ are 2.37 ± 0.003 GHz/kOe, 2.40 ± 0.001 GHz/kOe, and 2.37 ± 0.003 GHz/kOe, and the values of $(\frac{\gamma}{2\pi})_\parallel$ are 2.33 ± 0.002 GHz/kOe, 2.37 ± 0.003 GHz/kOe, and 2.29 ± 0.004 GHz/kOe in the 10-, 20-, and 30-nm-thick films, respectively. The $g_\perp$ and the $g_\parallel$ in various thicknesses of the TmBiIG film are determined by **Eq. 8**:

$$g = \frac{\gamma\hbar}{\mu_B}, \tag{8}$$

where $\hbar$ is the reduced Planck constant and μ_B is the Bohr magneton. A similar tendency is observed in all thickness samples, in which the $g_\perp$ is larger than $g_\parallel$. The discrepancy of the Landé g-factor in every sample is demonstrated in **Table 2**, which reveals the anisotropy of the Landé g-factor in the TmBiIG film.

Based on the Bruno theory (Bruno, 1989) and the Justin M. Shaw experiments (Shaw et al., 2013), when the Curie temperature (T_C) of the material is much higher than the room temperature, the asymmetric g-factor between the hard axis and the easy axis indicates the asymmetry of the orbital magnetic moment, confirming that the TmBiIG film has a perpendicular anisotropy along the easy axis, as demonstrated in **Eqs 9**, **10**:

$$\mathrm{MAE} = -A\frac{\xi}{4\mu_B}\Delta\mu_L, \tag{9}$$

$$\Delta\mu_L = \mu_L^\perp - \mu_L^\parallel = \frac{\mu_S}{2}(g^\perp - g^\parallel), \tag{10}$$

where ξ is the spin–orbit coupling parameter, A is a pre-factor which is a function of the electronic structure, and μ_B is the Bohr magneton. The Landé g-factor of the TmBiIG films is much lower than that of free electrons, indicating the mixing of orbital magnetism caused by the coupling of high spin–orbits from heavy elements Tm and Bi (Crossley et al., 2019).

Gilbert damping factor α and the FMR linewidth ΔH are usually used to characterize the magnetic dissipation. Damping parameter α from in-plane FMR usually includes a contribution from the non-Gilbert relaxation, namely, two-magnon scattering (Woltersdorf et al., 2009; Khodadadi et al., 2020) driven by defects, which broadens the ΔH as shown in **Figure 7**. However, two-magnon scattering is suppressed when the film is magnetized out-of-plane. The value of α is evaluated from the frequency dependence of the ΔH when an out-of-plane magnetic field is applied to the films. For the various thicknesses of films, α and ΔH_0 were extracted from the slope and the intercept with the *y*-axis using the following **Eq. 11**:

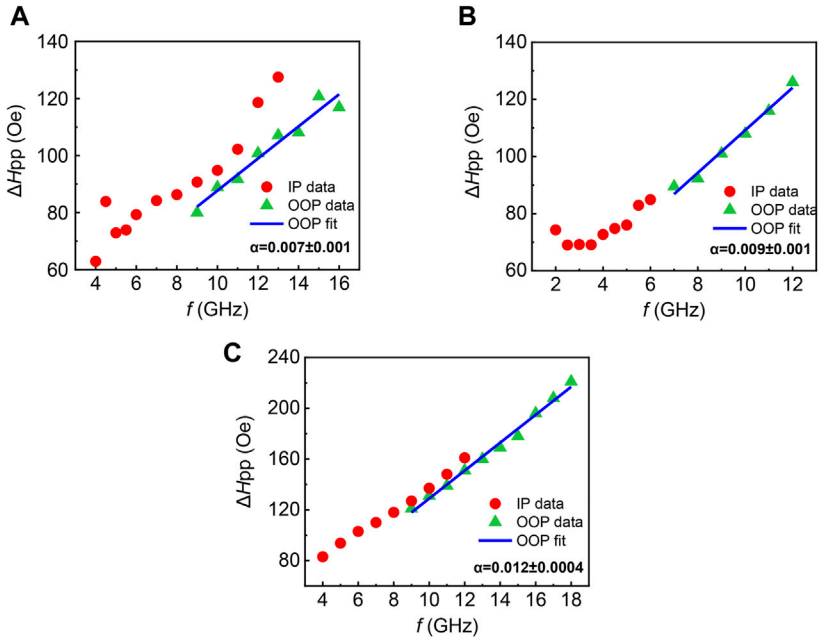

FIGURE 7 | Relationship between the frequency and the FMR linewidth in **(A)** 10-, **(B)** 20-, and **(C)** 30-nm-thick samples under in-plane and out-of-plane magnetized condition. The Gilbert damping factor in each thickness film and its error bar are shown in the figure, respectively.

$$\Delta H = \Delta H_0 + \frac{4\pi\alpha}{\gamma} f. \quad (11)$$

The values of Gilbert damping α in 10-, 20-, and 30-nm-thick TmBiIG films are 0.007 ± 0.001, 0.009 ± 0.001, and 0.012 ± 0.004, demonstrating that the TmBiIG/sGGG system is of the same order as that of the TmIG/sGGG system, which has been recently reported to be in the range of 0.015–0.025 (Ciubotariu et al., 2019), suggesting that the doping of Bi element has no significant influence on α. In addition, no clear thickness dependence of the damping constant was observed.

CONCLUSION

In summary, in this work, ultrathin TmBiIG films with strong PMA were fabricated on [111]-oriented sGGG substrate using pulsed laser deposition. The perpendicular anisotropic field of TmBiIG films with different thicknesses was determined by ferromagnetic resonance measurements. The anisotropic gyromagnetic ratio and the anisotropic g-factor are extracted from the in-plane and the out-of-plane FMR measurements, respectively. The appearance of the spin-wave mode in-plane is also related to the strong perpendicular anisotropy. The outstanding PMA effect and the relatively small Gilbert damping (α) indicate the potential application of the ultrathin TmBiIG films in the field of spintronic devices.

DATA AVAILABILITY STATEMENT

The original contributions presented in the study are included in the article/Supplementary Material, further inquiries can be directed to the corresponding authors.

AUTHOR CONTRIBUTIONS

XZ performed sample preparation and wrote the manuscript; LJ designed and supervised this work; DZ and LZ performed FMR measurements; XT and ZZ took part in data analysis; HM and BL provided editing and writing assistance. All authors read and contributed to the manuscript.

FUNDING

This work was supported by the National Key Research and Development Plan under Grant No. 2016YFA0300801, National Key Scientific Instrument and Equipment Development Project No. 51827802, the National Natural Science Foundation of China under Grant No. 62171096, and the Sichuan Science and Technology Support Project under Grant Nos. 2021YFG0347 and 2021YFG0091.

REFERENCES

Ahmed, A. S., Lee, A. J., Bagues, N., McCullian, B. A., Thabt, A. M. A., Perrine, A., et al. (2019). Spin-Hall Topological Hall Effect in Highly Tunable Pt/Ferrimagnetic-Insulator Bilayers. *Nano Lett.* 19, 2265. doi:10.1021/acs.nanolett.9b02265

Avci, C. O., Quindeau, A., Pai, C.-F., Mann, M., Caretta, L., Tang, A. S., et al. (2017). Beach, Current-Induced Switching in a Magnetic Insulator. *Nat. Mater.* 16, 309. doi:10.1038/nmat4812

Barsukov, I., Fu, Y., Gonçalves, A. M., Spasova, M., Farle, M., Sampaio, L. C., et al. (2014). Field-dependent Perpendicular Magnetic Anisotropy in CoFeB Thin Films. *Appl. Phys. Lett.* 105, 152403. doi:10.1063/1.4897939

Bruno, P. (1989). Tight-binding Approach to the Orbital Magnetic Moment and Magnetocrystalline Anisotropy of Transition-Metal Monolayers. *Phys. Rev. B: Condens. Matter Mater. Phys.* 39, 865. doi:10.1103/physrevb.39.865

Ciubotariu, O., Semisalova, A., Lenz, K., and Albrecht, M. (2019). Strain-induced Perpendicular Magnetic Anisotropy and Gilbert Damping of $Tm_3Fe_5O_{12}$ Thin Films. *Sci. Rep.* 9, 17474. doi:10.1038/s41598-019-53255-6

Crossley, S., Quindeau, A., Swartz, A. G., Rosenberg, E. R., Beran, L., Avci, C. O., et al. (2019). Ferromagnetic Resonance of Perpendicularly Magnetized Tm3Fe5O12/Pt Heterostructures. *Appl. Phys. Lett.* 115, 172402. doi:10.1063/1.5124120

Devolder, T., Couet, S., Swerts, J., and Kar, G. S. (2018). Gilbert Damping of High Anisotropy Co/Pt Multilayers. *J. Phys. D: Appl. Phys.* 51, 135002. doi:10.1088/1361-6463/aaaf30

Dötsch, H., Röschmann, P., and Schilz, W. (1978). Ferrimagnetic Resonance Spectra of Magnetic Bubble Films at Low Microwave Frequencies. *Appl. Phys. A: Mater. Sci. Process.* 15, 167.

Farle, M. (1998). Ferromagnetic Resonance of Ultrathin Metallic Layers. *Rep. Prog. Phys.* 61, 755. doi:10.1088/0034-4885/61/7/001

Fu, J., Hua, M., Wen, X., Xue, M., Ding, S., Wang, M., et al. (2017). Epitaxial Growth of $Y_3Fe_5O_{12}$ Thin Films with Perpendicular Magnetic Anisotropy. *Appl. Phys. Lett.* 110. doi:10.1063/1.4983783

Glowinski, H., Zywczak, A., Wrona, J., Krysztofik, A., Goscianska, I., Stobiecki, T., et al. (2017). CoFeB/MgO/CoFeB Structures with Orthogonal Easy Axes: Perpendicular Anisotropy and Damping. *J. Phys. Condens. Matter* 29, 485803.

Hansen, P., and Krumme, J. P. (1984). Magnetic and Magneto-Optical Properties of Garnet Films. *Thin Solid Films* 114, 69. doi:10.1016/0040-6090(84)90337-7

Hansen, P., and Witter, K. (1985). Growth-induced Uniaxial Anisotropy of Bismuth-Substituted Iron-Garnet Films. *J. Appl. Phys.* 58, 454. doi:10.1063/1.335645

Hansen, P., Witter, K., and Tolksdorf, W. (1983). Magnetic and Magneto-Optic Properties of lead- and Bismuth-Substituted Yttrium Iron Garnet Films. *Phys. Rev. B* 27, 6608. doi:10.1103/physrevb.27.6608

He, C., Navabi, A., Shao, Q., Yu, G., Wu, D., Zhu, W., et al. (2016). Spin-torque Ferromagnetic Resonance Measurements Utilizing Spin Hall Magnetoresistance in W/Co40Fe40B20/MgO Structures. *Appl. Phys. Lett.* 109, 202404. doi:10.1063/1.4967843

Hoekstra, B., van Stapele, R. P., and Robertson, J. M. (1977). Spin-wave Resonance Spectra of Inhomogeneous Bubble Garnet Films. *J. Appl. Phys.* 48, 382. doi:10.1063/1.323339

Illig, A. J., Chantler, C. T., and Payne, A. T. (2013). Voigt Profile Characterization of copperKα. *J. Phys. B: Mol. Opt. Phys.* 46, 235001. doi:10.1088/0953-4075/46/23/235001

Khodadadi, B., Rai, A., Sapkota, A., Srivastava, A., Nepal, B., Lim, Y., et al. (2020). Conductivitylike Gilbert Damping Due to Intraband Scattering in Epitaxial Iron. *Phys. Rev. Lett.* 124, 157201. doi:10.1103/physrevlett.124.157201

Kikkawa, T., Uchida, K., Shiomi, Y., Qiu, Z., Hou, D., Tian, D., et al. (2013). Longitudinal Spin Seebeck Effect Free from the Proximity Nernst Effect. *Phys. Rev. Lett.* 110, 067207. doi:10.1103/PhysRevLett.110.067207

Kubota, M., Shibuya, K., Tokunaga, Y., Kagawa, F., Tsukazaki, A., Tokura, Y., et al. (2013). Systematic Control of Stress-Induced Anisotropy in Pseudomorphic Iron Garnet Thin Films. *J. Magn. Magn. Mater.* 339, 63. doi:10.1016/j.jmmm.2013.02.045

Li, M., Jin, L., Zhong, Z., Tang, X., Yang, Q., Zhang, L., et al. (2020). Impact of Interfacial Chemical State on Spin Pumping and Inverse Spin Hall Effect in YIG/Pt Hybrids. *Phys. Rev. B* 102, 174435. doi:10.1103/physrevb.102.174435

Lin, Y., Jin, L., Zhang, H., Zhong, Z., Yang, Q., Rao, Y., et al. (2020). Bi-YIG Ferrimagnetic Insulator Nanometer Films with Large Perpendicular Magnetic Anisotropy and Narrow Ferromagnetic Resonance Linewidth. *J. Magn. Magn. Mater.* 496, 165886. doi:10.1016/j.jmmm.2019.165886

Portis, A. M. (1963). Low-Lying Spin Wave Modes in Ferromagnetic Films. *Appl. Phys. Lett.* 2, 69. doi:10.1063/1.1753779

Shao, Q., Liu, Y., Yu, G., Kim, S. K., Che, X., Tang, C., et al. (2019). Topological Hall Effect at above Room Temperature in Heterostructures Composed of a Magnetic Insulator and a Heavy Metal. *Nat. Electron.* 2, 182. doi:10.1038/s41928-019-0246-x

Shaw, J. M., Nembach, H. T., and Silva, T. J. (2013). Measurement of Orbital Asymmetry and Strain in $Co_{90}Fe_{10}$/Ni Multilayers and Alloys: Origins of Perpendicular Anisotropy. *Phys. Rev. B* 87, 054416. doi:10.1103/physrevb.87.054416

Shaw, J. M., Nembach, H. T., Weiler, M., Silva, T. J., Schoen, M., Sun, J. Z., et al. (2015). Perpendicular Magnetic Anisotropy and Easy Cone State in Ta/Co60Fe20B20/MgO. *IEEE Magn. Lett.* 6, 1. doi:10.1109/lmag.2015.2438773

Sokolov, N. S., Fedorov, V. V., Korovin, A. M., Suturin, S. M., Baranov, D. A., Gastev, S. V., et al. (2016). Thin Yttrium Iron Garnet Films Grown by Pulsed Laser Deposition: Crystal Structure, Static, and Dynamic Magnetic Properties. *J. Appl. Phys.* 119, 023903. doi:10.1063/1.4939678

Soumah, L., Beaulieu, N., Qassym, L., Carretero, C., Jacquet, E., Lebourgeois, R., et al. (2018). Ultra-low Damping Insulating Magnetic Thin Films Get Perpendicular. *Nat. Commun.* 9, 3355. doi:10.1038/s41467-018-05732-1

Tang, C., Sellappan, P., Liu, Y., Xu, Y., Garay, J. E., and Shi, J. (2016). Anomalous Hall Hysteresis in $Tm_3Fe_5O_{12}$/Ptwith Strain-Induced Perpendicular Magnetic Anisotropy. *Phys. Rev. B* 94, 140403. doi:10.1103/physrevb.94.140403

Tivakornsasithorn, K., Liu, X., Li, X., Dobrowolska, M., and Furdyna, J. K. (2014). Magnetic Anisotropy in Ultrathin Fe Films on GaAs, ZnSe, and Ge (001) Substrates. *J. Appl. Phys.* 116, 043915. doi:10.1063/1.4891253

Vilela, G., Chi, H., Stephen, G., Settens, C., Zhou, P., Ou, Y., et al. (2020). Strain-tuned Magnetic Anisotropy in Sputtered Thulium Iron Garnet Ultrathin Films and TIG/Au/TIG Valve Structures. *J. Appl. Phys.* 127, 115302. doi:10.1063/1.5135012

Woltersdorf, G., Kiessling, M., Meyer, G., Thiele, J. U., and Back, C. H. (2009). Damping by Slow Relaxing Rare Earth Impurities in $Ni_{80}Fe_{20}$. *Phys. Rev. Lett.* 102, 257602. doi:10.1103/physrevlett.102.257602

Wu, C. N., Tseng, C. C., Lin, K. Y., Cheng, C. K., Yeh, S. L., Fanchiang, Y. T., et al. (2018). High-quality Single-crystal Thulium Iron Garnet Films with Perpendicular Magnetic Anisotropy by off-axis Sputtering. *AIP Adv.* 8, 055904. doi:10.1063/1.5006673

Zanjani, S. M., and Onbasli, M. C. (2019). Thin Film Rare Earth Iron Garnets with Perpendicular Magnetic Anisotropy for Spintronic Applications. *AIP Adv.* 9, 035024. doi:10.1063/1.5079738

Conflict of Interest: The authors declare that the research was conducted in the absence of any commercial or financial relationships that could be construed as a potential conflict of interest.